

Fast Volume Alignment by Frequency-Marched Newton

Fabian Kruse¹, Valentin Debarnot², Vinith Kishore¹, and Ivan Dokmanić¹

¹Department of Mathematics and Computer Science, University of Basel, Basel, 4051, Switzerland

²INSA-Lyon, Universite Claude Bernard Lyon 1, CNRS, Inserm, CREATIS UMR 5220, U1294, Lyon, France

Abstract

We develop a fast and accurate method for 3D alignment, recovering the rotation and translation that best align a reference volume with a noisy observation. Classical matched filtering evaluates cross-correlation over a large discretized transformation space; we show that high-precision alignment can be achieved far more efficiently by treating pose estimation as a continuous optimization problem. Our starting point is a band-limited Wigner– D expansion of the rotational correlation, which enables rapid evaluation and efficient closed-form gradients and Hessians. Combined with analytical control of the complexity of trigonometric-polynomial landscapes, this makes second-order optimization practical in a setting where it is often avoided due to nonconvexity and noise sensitivity. We show that Newton-type refinement is stable and effective when initialized at low angular bandwidth: a coarse low-resolution $\text{SO}(3)$ search provides robust candidates, which are then refined by iterative frequency marching and Newton steps, with translations updated via FFT in an alternating scheme. We provide a deterministic convergence guarantee showing that, under verifiable spectral-decay and gap conditions, the frequency-marching scheme returns a near-optimal solution whose suboptimality is controlled by the Newton tolerance. On synthetic rotation-estimation benchmarks, the method attains sub-degree accuracy while substantially reducing runtime relative to exhaustive $\text{SO}(3)$ search. Integrated into the subtomogram-averaging pipeline of RELION5, it matches the baseline reconstruction quality, reaching local resolution at the Nyquist limit, while reducing pose-refinement time by more than an order of magnitude.

1 Introduction

We consider the problem of determining the pose—rotation and translation—of a particle within a three-dimensional volume, under severe noise and experimental artifacts. Our primary motivation comes from subtomogram averaging (STA) in cryogenic electron tomography (cryo-ET), where highly accurate particle alignment is essential to achieve high resolution. In practice, alignment is executed once per particle (and often iteratively), which makes even modest per-particle cost compound and motivates the search for methods that are both accurate and computationally efficient.

A classical approach to this problem is *matched filtering*, which seeks the transformation that maximizes the correlation between a reference template and the observed data. Matched filtering is known to be optimal for detecting a deterministic signal corrupted by additive white Gaussian noise, in the sense that it maximizes the output signal-to-noise ratio [1, 2, 3].

Let $g \in \mathcal{G}$ denote the unknown transformation to recover. The matched filtering objective is the correlation

$$C(g) \stackrel{\text{def.}}{=} \langle f, g \circ h \rangle = \int_{\mathbb{R}^d} f(x) \overline{(g^{-1}h)(x)} dx, \quad (1)$$

where $f, h : \mathbb{R}^d \rightarrow \mathbb{R}$ denote the noisy measurement and the reference template, respectively, with $d \geq 1$; in this paper $d = 3$. The pose estimation problem can then be formulated as

$$g^* \in \operatorname{argmax}_{g \in \mathcal{G}} C(g). \quad (2)$$

A straightforward strategy is to evaluate C over a suitable discretization of \mathcal{G} . This may be effective for a coarse search over low-dimensional pose spaces but it suffers from poor scaling as accuracy

requirements or the dimensionality increase. In favorable cases—namely when the transformation group \mathcal{G} admits a sampling theorem on a structured grid and the correlation can be expressed as a group convolution—FFT-based harmonic transforms allow fast evaluation on that grid. This is the case for translations (via the Euclidean FFT) and for rotations on $\text{SO}(3)$ (via Wigner/ $\text{SO}(3)$ FFTs) [4, 5]. However, accuracy is fundamentally limited by grid resolution, which is tied to the frequency bandwidth of the representation. Improving accuracy therefore requires finer discretizations and higher bandwidths, leading to substantially higher computational and memory costs despite the favorable asymptotic scaling of FFTs.

An alternative is to treat pose estimation as a *continuous optimization problem* over \mathcal{G} . When \mathcal{G} has a differentiable structure—such as $\text{SO}(3)$ or \mathbb{R}^3 —the correlation function admits well-defined gradients and Hessians, enabling efficient gradient-based and second-order optimization methods. This is, however, rarely done: the correlation landscape is highly non-convex with many spurious local maxima, and it becomes increasingly ill-conditioned at high resolution, in the sense that the local curvature near prominent maxima becomes highly anisotropic (i.e., the Hessian has a large condition number), making second-order steps sensitive to noise and numerical error. Success thus depends on effective initialization.

To address this challenge, we exploit the fact that smoother input volumes induce smoother correlation landscapes. Because correlation is a linear operation, band-limiting the inputs to angular degree L produces a band-limited correlation objective C_L on $\text{SO}(3)$. Lower L yields a simpler landscape with typically fewer critical points and lower curvature, so the basin of attraction of the global maximizer can be identified via a coarse search at moderate cost.

We call the resulting procedure *Matcha*. Matcha first performs a coarse exhaustive search at low bandwidth L_0 to identify a set of candidate rotations. The bandwidth is then progressively increased through a schedule $L_0 < L_1 < \dots < L_J$ —a strategy called *frequency marching*—and at each stage the candidates are refined via Newton steps on C_{L_j} , initialized from the previous level. At low and intermediate bandwidths, the correlation landscape is smooth and well-conditioned, allowing rapid convergence—typically 1–2 Newton steps per bandwidth suffice (Section 4). Because \mathcal{G} is low-dimensional (three-dimensional for $\text{SO}(3)$), the Hessian is a 3×3 matrix and can be inverted in closed form. By confining exhaustive search to a single low-frequency stage and using continuous optimization for refinement, this approach achieves sub-degree angular precision at substantially reduced computational cost compared with exhaustive high-resolution search. By confining exhaustive search to a single low-frequency stage and using continuous optimization for refinement, this approach achieves sub-degree angular precision at substantially reduced computational cost compared with exhaustive high-resolution search. Crucially, the final accuracy is determined by the continuous refinement, not by the resolution of the initial grid—so Matcha can achieve precision far beyond what the coarse $\text{SO}(3)$ -FFT grid alone would permit. Figure 1 illustrates the principle behind Matcha. At low frequencies, the correlation landscape is smooth and contains few local maxima, enabling reliable coarse search. As higher frequencies are introduced, the landscape becomes increasingly oscillatory. By tracking dominant maxima across bandwidths and refining them via local optimization, we recover the optimal pose without exhaustive search at full resolution.

1.1 Related work

Estimating three-dimensional rotations is a fundamental problem in imaging and signal processing. In electron tomography, this task is typically addressed through exhaustive search, which becomes computationally prohibitive at high angular resolution, especially when combined with the estimation of three-dimensional translations. A standard strategy is to leverage fast Fourier transforms on transformation spaces [6]. S2FFT [7, 5] provides accelerated harmonic transforms both on the sphere and on $\text{SO}(3)$; more broadly, FFTs on $\text{SO}(3)$ based on Wigner- D expansions enable fast evaluation of correlations over dense rotational grids [4]. These methods remain expensive, however, in large-scale problems such as cryo-ET subtomogram averaging. Our implementation builds upon the ball-harmonics expansion routines of Kileel et al. [8], extending their framework with a fully GPU-integrated PyTorch pipeline and accelerated NUFFT-based projections via cuFINUFFT [9], enabling efficient batched processing on modern GPUs.

In the context of STA for cryo-ET, a major challenge is the joint estimation of both unknown orientations and three-dimensional translations. This problem has traditionally been addressed through exhaustive sampling that combines fast Fourier transforms over rotations and spatial shifts [10, 11, 12].

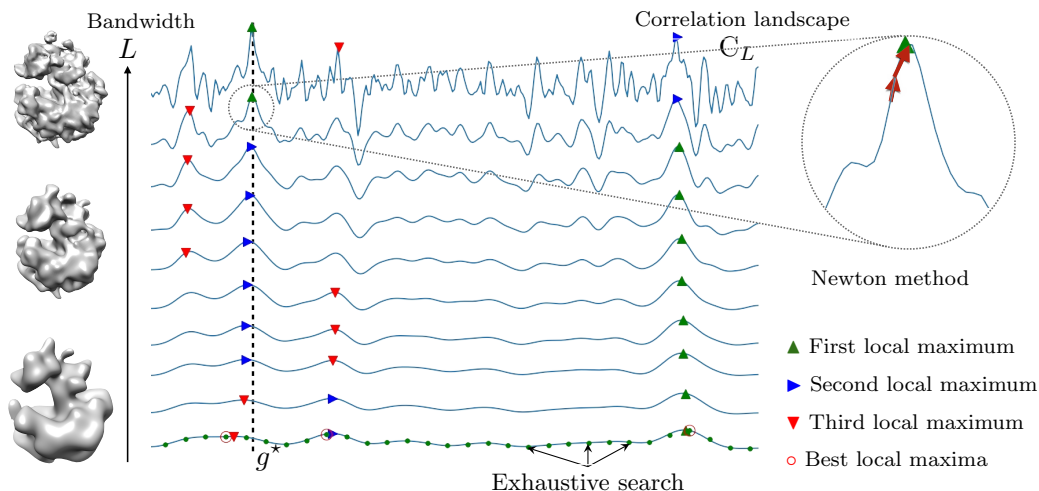


Figure 1: Evolution of a 1D correlation landscape under progressive bandwidth expansion. Each curve corresponds to a different bandwidth, with lower bandwidths producing smoother objectives and typically fewer local maxima. A coarse exhaustive search (evaluated on a discretization depicted in green) at low bandwidth identifies local maxima. As the bandwidth increases, these local maxima are tracked across scales using frequency marching, while local optimization refines the solution at each stage. This strategy avoids exhaustive search on highly oscillatory high-frequency landscapes while achieving high-precision alignment. For physical interpretation of low-pass filtering the correlation, we display correspondingly low-pass filtered copies of a particle on the left.

Several extensions incorporate physical characteristics of the imaging process, including the missing wedge [13] and spatially varying density variance [14]. Chen et al. [15] introduce a fast reference-free subtomogram alignment method that avoids an external template by iteratively aligning subtomograms to one another.

Continuous pose refinement has also been explored in cryo-EM. Zehni et al. [16] use alternating gradient-based optimization and ADMM for joint map-orientation estimation. This approach addresses the full reconstruction problem rather than the isolated rotational correlation considered here, and does not use second-order refinement or frequency marching. Related coarse-to-fine ideas do appear elsewhere in cryo-EM: Barnett et al. [17] propose a frequency-marching strategy for *ab initio* single-particle reconstruction, marching outward in Fourier radius from low to high frequency. Our use of frequency marching differs in both setting and scope: we apply it to band-limited rotational correlation on $SO(3)$, use it to track candidate basins via Newton refinement, and provide deterministic conditions under which basin tracking succeeds.

1.2 Paper outline

Section 2 introduces the frequency-marched alignment algorithm, including the low-frequency exhaustive search and the second-order continuous optimization. In Section 3, we establish sufficient conditions—formulated in terms of spectral decay and inter-basin gaps—under which Matcha is guaranteed to track the globally optimal basin through the bandwidth schedule and return a near-optimal estimate; we also quantify the advantage of marching over a single bandwidth jump. In Section 4, we evaluate accuracy and runtime on synthetic benchmarks, demonstrating speedups of several orders of magnitude over exhaustive search for isolated rotation estimation at varying SNR, and showing that the method is broadly applicable to any domain requiring fast $SO(3)$ correlation. We then integrate Matcha into a cryo-ET subtomogram averaging pipeline. On experimental data comprising approximately 21,000 subtomograms, we demonstrate that fast sub-degree rotational refinement enables STA reconstructions approaching the Nyquist limit (3.8 Å), while reducing alignment runtime by an order of magnitude compared with RELION5’s built-in refinement.

2 Method

We start by introducing the alignment problem and its spectral formulation; we then present our coarse-to-fine optimization strategy. Motivated by subtomogram alignment in cryo-electron tomography, we focus on $\mathcal{G} = \text{SO}(3)$. The full alignment problem also includes translations; for ease of exposition we defer their treatment to Appendix C.

We parameterize rotations $g \in \mathcal{G}$ by ZYZ Euler angles following [4],

$$g \equiv g(\alpha, \beta, \gamma) = r_z(\alpha)r_y(\beta)r_z(\gamma), \quad (3)$$

where

$$r_z(\alpha) = \begin{pmatrix} \cos \alpha & -\sin \alpha & 0 \\ \sin \alpha & \cos \alpha & 0 \\ 0 & 0 & 1 \end{pmatrix}, \quad r_y(\beta) = \begin{pmatrix} \cos \beta & 0 & \sin \beta \\ 0 & 1 & 0 \\ -\sin \beta & 0 & \cos \beta \end{pmatrix},$$

and $(\alpha, \beta, \gamma) \in [0, 2\pi) \times [0, \pi] \times [0, 2\pi)$. The rotation $g \in \mathcal{G}$ acts on a function $f : \mathbb{R}^3 \rightarrow \mathbb{R}$ as

$$(g \circ f)(x) = f(g^{-1}x).$$

We let $\mathcal{B}_3 \subset \mathbb{R}^3$ denote the unit ball and let $f, h \in L^2(\mathcal{B}_3)$ denote the observed subtomogram and the reference template, respectively. We define the $L^2(\mathcal{B}_3)$ inner product by $\langle f, h \rangle \stackrel{\text{def.}}{=} \int_{\mathcal{B}_3} f(x) \overline{h(x)} dx$.

The orientation estimation problem is formulated as

$$\hat{g} \in \underset{g \in \mathcal{G}}{\text{argmax}} C(g), \quad C(g) \stackrel{\text{def.}}{=} \langle f, g \circ h \rangle. \quad (4)$$

2.1 Ball-harmonic decomposition of the rotational cross-correlation

We decompose f and h in a ball-harmonic basis, which separates radial and angular variables. Under a rotation, the radial basis functions remain unchanged, while for each degree l , the spherical-harmonic coefficients are mixed by the Wigner- D matrices. After summing over the radial index, the rotational cross-correlation can therefore be expressed as a Fourier series on $\text{SO}(3)$ in the Wigner- D basis.

Truncating the angular content at degree L , we approximate the rotational cross-correlation (4) by

$$C_L(g) \stackrel{\text{def.}}{=} \sum_{l=0}^L \sum_{|m| \leq l} \sum_{|m'| \leq l} \sigma_{l,m,m'} D_{m,m'}^l(g), \quad g \in \mathcal{G}. \quad (5)$$

Here $D_{m,m'}^l$ are the matrix coefficients of the irreducible unitary representation of $\text{SO}(3)$ of degree l . By the Peter-Weyl theorem, they form the analogue of the Fourier basis on $\text{SO}(3)$. The expansion in (5) is therefore a Fourier series for the rotational cross-correlation, and truncation at degree L amounts to retaining only frequencies up to L . In particular, $C_L \rightarrow C$ in $L^2(\text{SO}(3))$ as $L \rightarrow \infty$.

For a fixed rotation g , a direct evaluation of (5) requires $\mathcal{O}(L^3)$ operations, since $\sum_{l=0}^L (2l+1)^2 = \mathcal{O}(L^3)$. This representation is also convenient for optimization: derivatives of C_L with respect to the rotation parameters can be obtained in closed form from the derivatives of Wigner- D matrices, with the same asymptotic cost as evaluating C_L itself.

In the proposed coarse-to-fine scheme, we start from a small cutoff L_0 —yielding a smoothed, low-angular-frequency objective—and progressively increase L , thereby enriching the angular content of $C_L(g)$. At each stage, the approximation at the new bandwidth is obtained simply by extending the sum over the precomputed coefficients $\sigma_{l,m,m'}$ to include higher degrees; no recomputation of lower-degree coefficients is needed.

2.2 Continuous optimization

Because the cross-correlation C is non-convex, it is in general impossible to find the global maximum of C directly by first or second order continuous optimization. It becomes possible, however, provided that a good initial estimate is available. Finding such an initial estimate is in turn easier for the bandlimited cross-correlation C_L , since lower-bandwidth functions generically have fewer critical points and a smoother landscape—thus a larger basin of attraction for the global maximum.

Once one decides to attempt a continuous refinement, a natural modern approach is to use automatic differentiation and gradient ascent: it only requires gradients and typically makes progress from relatively crude initializations. On landscapes such as bandlimited trigonometric polynomials, however, second-order methods can be orders of magnitude faster, since gradient-based methods may require many small steps to exploit curvature information. This becomes especially relevant in our setting, where the cost of evaluating the objective and its derivatives is dominated by the same $\mathcal{O}(L^3)$ Wigner- D terms, making the asymptotic cost complexity scaling in terms of L the same for both first- and second-order methods. Moreover, because \mathcal{G} has a fixed, low dimension (three for $\text{SO}(3)$), the Newton step only requires inverting a 3×3 matrix, which can be done in closed form.

Iteration count is therefore the main factor determining the difference in runtime. Gradient ascent typically requires many more iterations to reach high precision, whereas Newton’s method typically converges in only a few iterations once initialized in the desired basin of attraction (see Figure 4c).

While $\text{SO}(3)$ admits an intrinsic Riemannian geometry (Riemannian gradient/Hessian and a retraction/ exponential-map update), we found that working in a local coordinate chart is sufficient in practice. In our implementation we optimize directly in wrapped Euler angles $\theta = (\alpha, \beta, \gamma)$ and map to rotations via $g(\theta)$. Since continuous optimization is initialized with a rotation near a maximizer, iterates remain in a local neighborhood where this parameterization is well-conditioned. In this chart, the update takes the familiar form

$$\theta^{t+1} = \theta^t - H_{C_L}^{-1}(\theta^t) \nabla C_L(\theta^t), \quad g^t = g(\theta^t),$$

where $H_{C_L}(\theta) \stackrel{\text{def.}}{=} \nabla^2 C_L(\theta)$ denotes the Hessian. We remark that closed-form derivatives are substantially more efficient than automatic differentiation in this setting: they avoid constructing and backpropagating through the Wigner- D matrices and provide direct access to the Hessian, enabling fast second-order refinement. The convergence analysis in Section 3 is formulated intrinsically on $\text{SO}(3)$; the Euler-angle parameterization is used only in the implementation.

2.3 Initialization via low-resolution $\text{SO}(3)$ -FFT

The success of continuous optimization depends on suitable initialization. We obtain one by performing a grid search on the low-bandwidth correlation C_{L_0} , which is smooth and inexpensive to evaluate.

We use an $\text{SO}(3)$ fast Fourier transform (SOFFT) [4, 18, 5] to evaluate C_{L_0} on a grid of $\mathcal{O}((KL_0)^3)$, where $K \geq 1$ is the oversampling factor. On the natural equiangular grid, classical algorithms achieve a complexity of $\mathcal{O}(L_0^4)$ [4]; with oversampling factor K and $M = (KL_0)^3$ target rotations, nonequispaced variants achieve $\mathcal{O}(M + L_0^4)$ [18], compared with $\mathcal{O}(M \cdot L_0^3)$ for direct evaluation. We retain the N_C strongest local maxima as candidate initializations; although their angular accuracy is limited by the grid spacing (a few degrees in our examples), it is sufficient to initialize the subsequent continuous optimization stages.

2.4 Coarse-to-fine optimization algorithm

The complete alignment procedure combines a single exhaustive search at L_0 with frequency-marched continuous optimization. The final estimate is reported at angular cutoff L_J , chosen such that C_{L_J} approximates the full correlation to the desired accuracy. Algorithm 1 summarizes the procedure.

In practice, we run at most M_{iter} Newton steps per band and terminate early when the gradient norm, the parameter increment, or the relative change in the objective fall below a prescribed tolerance. We use a fixed bandwidth schedule starting from $L_0 = 30$, for which the exhaustive $\text{SO}(3)$ -FFT search remains inexpensive, and ending at the target bandwidth L_J . Intermediate bandwidths are chosen to keep the per-step perturbation within the stability bounds of our convergence analysis (Section 3.4). We retain $N_C = 10$ candidates with oversampling factor $K = 2$ for the initial SOFFT search. Newton refinement is preferable to gradient ascent because both methods have the same asymptotic per-iteration cost, while Newton typically reaches high precision in substantially fewer iterations once initialized in the correct basin (see Figure 4c).

Algorithm 1 Matcha, a Multi-band Angular Template Matching Algorithm

Require: Angular cutoffs $\{L_0, L_1, \dots, L_J\}$

Require: Number of Newton iterations M_{iter}

Require: Number of candidates N_C

Require: Oversampling factor K

- 1: Perform exhaustive search with SOFFT at angular cutoff L_0 with oversampling factor K
 - 2: Retain the N_C strongest local maxima $\{g_n^{(0)}\}_{n=1}^{N_C}$
 - 3: **for** j in $\{1, \dots, J\}$ **do**
 - 4: **for** n in $\{1, \dots, N_C\}$ **do**
 - 5: $g_n^{(j)} \leftarrow$ result of M_{iter} Newton steps on C_{L_j} initialized at $g_n^{(j-1)}$
 - 6: **end for**
 - 7: **end for**
 - 8: **return** $\operatorname{argmax}_{n \in \{1, \dots, N_C\}} C_{L_J}(g_n^{(J)})$
-

3 Theoretical analysis

The efficiency of Matcha (Algorithm 1) results from several factors: typical correlation landscapes are benign and evolve smoothly over bandwidths, the overall problem is low-dimensional with a controlled number of local maxima to track, all objects involved in the second-order optimization are available in efficient closed form, and second order optimization is locally very fast.

In this section we prove that Algorithm 1 (approximately) recovers the global maximum of the correlation under suitable assumptions. Given these assumptions, our result is deterministic. It is possible that stronger guarantees can be given “with high probability” over a suitable ensemble of random particles, but we leave this to future work.

Our proof strategy relies on the intuition that the position of local maxima does not change much if the bandwidth L is increased by a little. Turning this intuition into a frequency-marching proof requires handling two main failure modes. One is that a tracked local maximum splits into two or more local maxima. The other is that as we increase the bandwidth, a new untracked local maximum emerges which eventually grows into a global maximum. We will make suitable assumptions under which this cannot happen.

3.1 Setting

We select a bandwidth schedule $L_0 < L_1 < \dots < L_J$ and write

$$F_j \stackrel{\text{def.}}{=} C_{L_j}, \quad j = 0, 1, \dots, J$$

for the correlation function at bandwidth L_j . In order to exclude the possibility that a new maximum emerges outside the tracked union of balls S and eventually becomes global, we will need to assume that the global maximum at bandwidth L_J is sufficiently prominent. A technical tool for this is the set gap.

Definition 3.1. *Let $F : \text{SO}(3) \rightarrow \mathbb{R}$ and $S \subset \text{SO}(3)$ be compact. The set gap of F with respect to S is*

$$\Gamma_F(S) \stackrel{\text{def.}}{=} \max_{g \in S} F(g) - \sup_{g \notin S} F(g). \quad (6)$$

Note that if $\Gamma_F(S) > 0$ then S contains a global maximum of F .

3.2 Failure mode elimination

The first lemma shows that under suitable assumptions (i.e. set gap and spectral decay with frequency) it is impossible that a maximum absent at bandwidth L_0 becomes global at bandwidth L_J .

Lemma 3.1 (Set-gap stability). *Let $F, \tilde{F} : \text{SO}(3) \rightarrow \mathbb{R}$ be continuous and let $S \subset \text{SO}(3)$ be compact. Assume the set gap $\Gamma_F(S)$ defined in (6) satisfies $\Gamma_F(S) > 0$. If*

$$\|F - \tilde{F}\|_\infty \leq \varepsilon \quad \text{and} \quad \varepsilon < \Gamma_F(S), \quad (7)$$

then every global maximizer $\tilde{g}^* \in \operatorname{argmax} \tilde{F}$ lies in S .

Proof. Define $a_S := \max_{g \in S} F(g)$ and $a_{S^c} := \sup_{g \notin S} F(g)$, so $a_S - a_{S^c} = \Gamma_F(S) > 0$ by assumption. Let g_S be such that $F(g_S) = a_S$ (it exists since S is a finite union of closed balls hence compact). For any $g \notin S$,

$$\tilde{F}(g) \leq F(g) + \varepsilon \leq a_{S^c} + \varepsilon \leq a_S - \Gamma_F(S) + \varepsilon, \quad (8)$$

and also

$$\tilde{F}(g_S) \geq F(g_S) - \varepsilon = a_S - \varepsilon.$$

Subtracting,

$$\tilde{F}(g_S) - \tilde{F}(g) \geq (a_S - \varepsilon) - (a_S - \Gamma_F(S) + \varepsilon) = \Gamma_F(S) - 2\varepsilon > 0.$$

Thus $\tilde{F}(g_S) > \tilde{F}(g)$ for $g \notin S$. In other words: any global maximizer of \tilde{F} must be in S . Since $\operatorname{SO}(3)$ is compact and \tilde{F} is continuous, \tilde{F} attains its maximum. \square

In practice, this lemma is a way to exploit the spectral decay with frequency. Concretely, if the high-frequency tail $\|C_{L_J} - C_{L_0}\|_\infty$ is smaller than half the set gap at bandwidth L_0 , then no newly born maximum outside the tracked union of balls S can become global.

Next we establish basin regularity.

Definition 3.2. *Strong concavity and smoothness* Let $U \subset \operatorname{SO}(3)$ be geodesically convex and $F \in C^2(U)$. We say F is μ -strongly concave and M -smooth on U if for every $g \in U$ and every unit tangent vector $X \in T_g \operatorname{SO}(3)$,

$$-M \leq \langle \nabla^2 F(g)[X], X \rangle \leq -\mu.$$

On any Riemannian manifold sufficiently small geodesic balls are geodesically convex.

Lemma 3.2 (Second-order two-sided bounds from a critical point). *Let U be geodesically convex, $F \in C^2(U)$, and let $g_0 \in U$ satisfy $\nabla F(g_0) = 0$. Assume F is μ -strongly concave and M -smooth on U . Then for every $g \in U$,*

$$F(g_0) - \frac{M}{2} d(g, g_0)^2 \leq F(g) \leq F(g_0) - \frac{\mu}{2} d(g, g_0)^2.$$

Proof. Fix $g \in U$ and let $\gamma : [0, \ell] \rightarrow U$ be the unit-speed minimizing geodesic from $\gamma(0) = g_0$ to $\gamma(\ell) = g$, so $\ell = d(g, g_0)$. Let $h(t) = F(\gamma(t))$. Then $h'(0) = \langle \nabla F(g_0), \dot{\gamma}(0) \rangle = 0$ and

$$h''(t) = \langle \nabla^2 F(\gamma(t))[\dot{\gamma}(t)], \dot{\gamma}(t) \rangle.$$

Since $\|\dot{\gamma}(t)\| = 1$ and F is μ -strongly concave and M -smooth, we have for all $t \in [0, \ell]$,

$$-M \leq h''(t) \leq -\mu.$$

Integrate $h''(t) \geq -M$ from 0 to t to get $h'(t) \geq -Mt$, and integrate again from 0 to ℓ :

$$h(\ell) - h(0) = \int_0^\ell h'(t) dt \geq \int_0^\ell (-Mt) dt = -\frac{M}{2} \ell^2.$$

Thus $h(\ell) \geq h(0) - \frac{M}{2} \ell^2$, i.e. $F(g) \geq F(g_0) - \frac{M}{2} d(g, g_0)^2$. The upper bound is identical using $h''(t) \leq -\mu$. \square

Lemma 3.3 (Basin persistence under a C^2 perturbation). *Let $U = \overline{B(g^*, r)}$ be a closed geodesically convex ball. Let $\Omega \subset \operatorname{SO}(3)$ be an open neighborhood of U , and let $F, E \in C^2(\Omega)$. Assume F is μ -strongly concave on U and that g^* is the necessarily unique maximizer of F on U . Let $\tilde{F} \stackrel{\text{def.}}{=} F + E$ and set*

$$a \stackrel{\text{def.}}{=} \|\nabla E\|_{L^\infty(U)}, \quad b \stackrel{\text{def.}}{=} \sup_{g \in U} \|\nabla^2 E(g)\|_{\text{op}}.$$

Assume $b < \mu$ and $a < (\mu - b)r/2$. Then \tilde{F} is $(\mu - b)$ -strongly concave on U with an unique maximizer $\tilde{g}^ \in \operatorname{int}(U)$ such that $d(\tilde{g}^*, g^*) \leq a/(\mu - b)$.*

Proof. To show strong concavity note that for any unit tangent X at any $g \in U$,

$$\left\langle \nabla^2 \tilde{F}(g)[X], X \right\rangle = \left\langle \nabla^2 F(g)[X], X \right\rangle + \left\langle \nabla^2 E(g)[X], X \right\rangle \leq -\mu + b = -(\mu - b).$$

By continuity and compactness, \tilde{F} attains a maximum on U . Because \tilde{F} is $(\mu - b)$ -strongly concave on the geodesically convex U , it can have *at most one* maximizer in U (if there were two, strict concavity along the connecting geodesic would be contradicted).

It remains to rule out a maximizer on ∂U . Let $\gamma : [0, r] \rightarrow \bar{U}$ be any unit-speed geodesic with $\gamma(0) = g^*$ and $\gamma(r) \in \partial U$. Define $h(t) = \tilde{F}(\gamma(t))$. Then $h'(0) = \left\langle \nabla \tilde{F}(g^*), \dot{\gamma}(0) \right\rangle = \langle \nabla E(g^*), \dot{\gamma}(0) \rangle$ so $|h'(0)| \leq a$. We already showed $h''(t) \leq -(\mu - b)$. Integrating $h''(t) \leq -(\mu - b)$ twice gives

$$h(r) \leq h(0) + r h'(0) - \frac{\mu - b}{2} r^2 \leq h(0) + ar - \frac{\mu - b}{2} r^2.$$

Since $a < (\mu - b)r/2$, we have $ar - \frac{\mu - b}{2} r^2 < 0$, hence $h(r) < h(0)$. Thus no boundary point can maximize \tilde{F} , so the maximizer lies in $\text{int}(U)$.

To bound the displacement, let \tilde{g}^* be the unique maximizer of \tilde{F} in U and $\gamma : [0, \ell] \rightarrow U$ the unit-speed minimizing geodesic from $\gamma(0) = g^*$ to $\gamma(\ell) = \tilde{g}^*$, so $\ell = d(g^*, \tilde{g}^*)$. Define $\psi(t) = \left\langle \nabla \tilde{F}(\gamma(t)), \dot{\gamma}(t) \right\rangle$. Then $\psi(\ell) = 0$ because $\nabla \tilde{F}(\tilde{g}^*) = 0$, and

$$\psi'(t) = \left\langle \nabla^2 \tilde{F}(\gamma(t))[\dot{\gamma}(t)], \dot{\gamma}(t) \right\rangle \leq -(\mu - b).$$

Integrating gives $0 = \psi(\ell) \leq \psi(0) - (\mu - b)\ell$, hence $(\mu - b)\ell \leq \psi(0)$. But $\psi(0) = \left\langle \nabla \tilde{F}(g^*), \dot{\gamma}(0) \right\rangle = \langle \nabla E(g^*), \dot{\gamma}(0) \rangle \leq \|\nabla E(g^*)\| \leq a$. Therefore $\ell \leq a/(\mu - b)$. \square

3.3 Main result

We now analyze the multi-band marching scheme in Algorithm 1: we start with a low-bandwidth exhaustive search at L_0 , keep $P = N_C$ candidate basins, and for $j = 1, \dots, J$ refine each candidate by M_{iter} Newton steps for $F_j = C_{L_j}$, then select the best candidate at L_j . The key proof obligations are: (i) basins do not split internally as j increases; (ii) no *untracked* maximum can become a global maximum at L_j ; (iii) because Newton is run for a finite number of steps, the output is only approximately optimal.

Assumption 3.1. We make the following assumptions

- (A) Tracked basins at L_0 and convexity radius. Fix $r > 0$ such that every closed geodesic ball $\overline{B}(g, \rho)$ with $\rho \leq r$ is geodesically convex. There exist points $g_{p,0} \in \text{SO}(3)$, $p = 1, \dots, P$, such that the closed balls

$$U_p \stackrel{\text{def.}}{=} \overline{B}(g_{p,0}, r) \subset \text{SO}(3), \quad p = 1, \dots, P,$$

are pairwise disjoint, and $g_{p,0}$ is the unique maximizer of F_0 on U_p . We let $S \stackrel{\text{def.}}{=} \bigcup_{p=1}^P U_p$.

- (B) Small per-step C^2 changes on S with non-degeneracy budget. For $j \geq 1$, let $E_j \stackrel{\text{def.}}{=} F_j - F_{j-1}$ and

$$a_j \stackrel{\text{def.}}{=} \|\nabla E_j\|_{L^\infty(S)}, \quad b_j := \sup_{g \in S} \|\nabla^2 E_j(g)\|_{\text{op}}, \quad \delta_j \stackrel{\text{def.}}{=} \|E_j\|_\infty.$$

We have

$$\sum_{j=1}^J b_j \leq \frac{\mu}{2}, \quad a_j < \frac{\mu r}{8}, \quad \sum_{j=1}^J \frac{2a_j}{\mu} \leq \frac{r}{2}, \quad (9)$$

and F_0 is μ -strongly concave on each U_p .

- (C) Set-gap prevents late-born global maximizers outside S . We have $\Gamma_{F_0}(S) > 0$ and

$$2 \sum_{j=1}^J \delta_j < \Gamma_{F_0}(S). \quad (10)$$

It thus follows $\|F_J - F_0\|_\infty \leq \sum_j \delta_j < \Gamma_{F_0}(S)/2$.

(D) Finite Newton accuracy. For each $j = 1, \dots, J$ and each p , after M_{iter} Newton steps on F_j initialized from the previous level, the returned iterate $g_p^{(j)}$ satisfies

$$d\left(g_p^{(j)}, m_{p,j}\right) \leq \tau, \quad \tau \leq \frac{r}{2} \quad (11)$$

where $m_{p,j}$ denotes the unique maximizer of F_j on U_p (whose existence/uniqueness is proved below).

(E) Final inter-basin winner is unique and separated. Define p^* so that

$$F_J(m_{p^*,J}) = \max_{p=1,\dots,P} F_J(m_{p,J}),$$

and assume this winner is unique. Let

$$\gamma \stackrel{\text{def.}}{=} F_J(m_{p^*,J}) - \max_{p \neq p^*} F_J(m_{p,J}) > 0.$$

(F) Curvature bound converts distance-to-optimum into value-to-optimum. Let

$$M_J \stackrel{\text{def.}}{=} \sup_{g \in S} \|\nabla^2 F_J(g)\|_{\text{op}} < \infty.$$

(finite because $F_J \in C^2$ and S is compact). The Newton tolerance satisfies

$$\frac{M_J}{2} \tau^2 \leq \frac{\gamma}{4}. \quad (12)$$

Theorem 3.4 (Main result). *The output of Matcha (Algorithm 1), $\hat{g} \in \operatorname{argmax}_{p=1,\dots,P} F_J(g_p^{(J)})$ is near-optimal; namely,*

$$d(\hat{g}, m_{p^*,J}) \leq \tau \quad \text{and} \quad 0 \leq \max_{g \in \text{SO}(3)} F_J(g) - F_J(\hat{g}) \leq \frac{M_J}{2} \tau^2.$$

Proof. Part (i): We start by proving existence/uniqueness of basin maximizers for all j , without splitting. Fix a basin index p . We prove by induction on j that F_j has a unique maximizer $m_{p,j} \in \text{int}(U_p)$ and that

$$d(m_{p,j}, m_{p,0}) \leq \sum_{k=1}^j \frac{2a_k}{\mu}. \quad (13)$$

Base $j = 0$ holds by Assumption (A). Induction step: assume the claim for $j - 1$. Let $\mu_{j-1} \stackrel{\text{def.}}{=} \mu - \sum_{k=1}^{j-1} b_k$. By Assumption (9), $\mu_{j-1} \geq \mu/2$. Because $F_{j-1} = F_0 + \sum_{k=1}^{j-1} E_k$ and $\|\nabla^2 E_k\|_{\text{op}} \leq b_k$ on S , we have on $U_p \subset S$ the concavity bound

$$\langle \nabla^2 F_{j-1}(g)[X], X \rangle \leq -\mu + \sum_{k=1}^{j-1} b_k = -\mu_{j-1},$$

so F_{j-1} is μ_{j-1} -strongly concave on U_p . In particular $m_{p,j-1}$ is the unique maximizer of F_{j-1} on U_p .

We will apply Lemma 3.3 on the smaller convex ball

$$U' \stackrel{\text{def.}}{=} \overline{B(m_{p,j-1}, r/2)}.$$

First, U' is geodesically convex because $r/2$ is below the convexity radius assumed in (A). Second, $U' \subset U_p$: indeed by (13) at level $j - 1$ and (9),

$$d(m_{p,j-1}, m_{p,0}) \leq \sum_{k=1}^{j-1} \frac{2a_k}{\mu} \leq \frac{r}{2},$$

hence for any $g \in U'$,

$$d(g, m_{p,0}) \leq d(g, m_{p,j-1}) + d(m_{p,j-1}, m_{p,0}) \leq \frac{r}{2} + \frac{r}{2} = r,$$

so $g \in U_p$.

On $U' \subset S$ we have $\|\nabla E_j\|_\infty \leq a_j$ and $\|\nabla^2 E_j\|_{\text{op}} \leq b_j$. To apply Lemma 3.3 with strong concavity constant μ_{j-1} and radius $r/2$, we need

$$b_j < \mu_{j-1} \quad \text{and} \quad a_j < (\mu_{j-1} - b_j) \frac{r}{4}.$$

But

$$\mu_{j-1} - b_j = \mu - \sum_{k=1}^j b_k \geq \mu - \sum_{k=1}^J b_k \geq \frac{\mu}{2},$$

so in particular $b_j < \mu_{j-1}$, and

$$(\mu_{j-1} - b_j) \frac{r}{4} \geq \frac{\mu r}{8}.$$

By (9), $a_j < \mu r/8$, hence the conditions of Lemma 3.3 are satisfied.

Lemma 3.3 therefore yields a maximizer $m_{p,j} \in \text{int}(U') \subset \text{int}(U_p)$ of F_j on U' , and in particular on U_p .

To see that $m_{p,j}$ is in fact the *unique* maximizer of F_j on all of U_p , note that for any $g \in U_p$ and any unit tangent $X \in T_g \text{SO}(3)$,

$$\langle \nabla^2 F_j(g)[X], X \rangle = \langle \nabla^2 F_0(g)[X], X \rangle + \sum_{k=1}^j \langle \nabla^2 E_k(g)[X], X \rangle \leq -\mu + \sum_{k=1}^j b_k.$$

By (9), $\sum_{k=1}^j b_k \leq \mu/2$, so F_j is $(\mu/2)$ -strongly concave on U_p and therefore has at most one maximizer on the geodesically convex U_p . Since $m_{p,j} \in U' \subset U_p$ is already a maximizer, it is the unique maximizer of F_j on U_p .

Lemma 3.3 gives

$$d(m_{p,j}, m_{p,j-1}) \leq \frac{a_j}{\mu_{j-1} - b_j} \leq \frac{a_j}{\mu/2} = \frac{2a_j}{\mu},$$

so (13) follows by summing in j .

Part (ii): We now show that global maximizers of F_J all lie in S (and are thus tracked combined with part (i)). We have

$$\|F_J - F_0\|_\infty = \left\| \sum_{j=1}^J E_j \right\|_\infty \leq \sum_{j=1}^J \|E_j\|_\infty = \sum_{j=1}^J \delta_j.$$

Assumption (10) gives $2\|F_J - F_0\|_\infty < \Gamma_{F_0}(S)$. Apply Lemma 3.1 with $F = F_0$, $\tilde{F} = F_J$, and this S . Then every global maximizer of F_J lies in S . This proves (ii).

Part (iii): By (ii), $\max_{\text{SO}(3)} F_J = \max_{g \in S} F_J(g) = \max_p \max_{g \in U_p} F_J(g) = \max_p F_J(m_{p,J})$. Let p^* be the unique maximizer index and $\gamma > 0$ the inter-basin gap. We first verify that the returned Newton point lies in the tracked basin. By (11) and the drift bound (13) (with $j = J$),

$$d(g_p^{(J)}, m_{p,0}) \leq d(g_p^{(J)}, m_{p,J}) + d(m_{p,J}, m_{p,0}) \leq \tau + \sum_{k=1}^J \frac{2a_k}{\mu} \leq \frac{r}{2} + \frac{r}{2} = r.$$

Hence $g_p^{(J)} \in U_p$. Now fix any p . Because $m_{p,J}$ maximizes F_J on U_p and $g_p^{(J)} \in U_p$,

$$F_J(g_p^{(J)}) \leq F_J(m_{p,J}). \tag{14}$$

On the other hand, for every $g \in U_p$ and every unit tangent vector $X \in T_g \text{SO}(3)$,

$$-M_J \leq \langle \nabla^2 F_J(g)[X], X \rangle \leq -\mu/2,$$

where the upper bound is the $(\mu/2)$ -strong concavity established in Part (i) and the lower bound holds by definition of M_J . Hence F_J is $(\mu/2)$ -strongly concave and M_J -smooth on U_p .

Applying Lemma 3.2 on U_p with $g_0 = m_{p,J}$ (noting $\nabla F_J(m_{p,J}) = 0$ since $m_{p,J} \in \text{int}(U_p)$) and using (11) gives the lower bound

$$F_J(g_p^{(J)}) \geq F_J(m_{p,J}) - \frac{M_J}{2}\tau^2. \quad (15)$$

For the winning basin p^* , (15) gives

$$F_J(g_{p^*}^{(J)}) \geq F_J(m_{p^*,J}) - \frac{M_J}{2}\tau^2.$$

For any other basin $p \neq p^*$, (14) and the definition of γ give

$$F_J(g_p^{(J)}) \leq F_J(m_{p,J}) \leq F_J(m_{p^*,J}) - \gamma.$$

Therefore

$$F_J(g_{p^*}^{(J)}) - F_J(g_p^{(J)}) \geq \gamma - \frac{M_J}{2}\tau^2.$$

By (12), $(M_J/2)\tau^2 \leq \gamma/4$, hence the difference is at least $3\gamma/4 > 0$. So the algorithm's final argmax over p must select p^* . Thus $\hat{g} = g_{p^*}^{(J)} \in U_{p^*}$ and $d(\hat{g}, m_{p^*,J}) \leq \tau$ by (11).

Part (iv): Finally, since $m_{p^*,J}$ is a global maximizer of F_J (from (ii) and the definition of p^*),

$$\max_{\text{SO}(3)} F_J - F_J(\hat{g}) = F_J(m_{p^*,J}) - F_J(\hat{g}).$$

Applying (15) with $p = p^*$ and $\hat{g} = g_{p^*}^{(J)}$ we get

$$F_J(\hat{g}) \geq F_J(m_{p^*,J}) - \frac{M_J}{2}\tau^2$$

implying

$$0 \leq F_J(m_{p^*,J}) - F_J(\hat{g}) \leq \frac{M_J}{2}\tau^2.$$

□

3.4 Benefits of marching

The assumptions of Theorem 3.4 are stated in terms of the abstract quantities a_j, b_j, δ_j . To connect these with the bandwidth schedule, we use the fact that bandlimited functions on $\text{SO}(3)$ satisfy Bernstein-type derivative bounds: higher derivatives are controlled by the bandwidth and the sup-norm of the function itself.

Lemma 3.5 (Bernstein inequality on $\text{SO}(3)$). *Let m be a fixed bi-invariant Riemannian metric on $\text{SO}(3)$, and let*

$$\Pi_L := \text{span}\{D_{m,m'}^\ell : 0 \leq \ell \leq L, |m| \leq \ell, |m'| \leq \ell\}.$$

Then there exist constants $B_1, B_2 > 0$, depending only on the metric normalization, such that every $F \in \Pi_L$ satisfies

$$\|\nabla F\|_{L^\infty(\text{SO}(3))} \leq B_1(1+L)\|F\|_{L^\infty(\text{SO}(3))},$$

and

$$\|\nabla^2 F\|_{L^\infty_{\text{op}}(\text{SO}(3))} \leq B_2(1+L)^2\|F\|_{L^\infty(\text{SO}(3))}.$$

Proof. Choose a fixed orthonormal basis of left-invariant vector fields X_1, X_2, X_3 for the metric m , and set

$$\mathcal{L} := -(X_1^2 + X_2^2 + X_3^2).$$

For a bi-invariant metric on $\text{SO}(3)$, the operator \mathcal{L} agrees with the Laplace–Beltrami operator up to a constant depending only on the metric normalization. Hence there exists $\kappa_n > 0$ such that each Wigner function $D_{m,m'}^\ell$ is an eigenfunction of \mathcal{L} with eigenvalue $\kappa_g \ell(\ell+1)$. Therefore

$$\Pi_L \subset E_{\kappa_g L(L+1)}(\mathcal{L}),$$

where $E_\lambda(\mathcal{L})$ denotes the span of the eigenspaces of \mathcal{L} with eigenvalue at most λ .

By Pesenson's Bernstein inequality on compact homogeneous manifolds, this implies

$$\max_i \|X_i F\|_\infty \leq C \sqrt{L(L+1)} \|F\|_\infty, \quad \max_{i,j} \|X_i X_j F\|_\infty \leq C L(L+1) \|F\|_\infty,$$

with a constant C depending only on the fixed metric normalization.

Since X_1, X_2, X_3 is an orthonormal frame, we have pointwise

$$|\nabla F|^2 = \sum_{i=1}^3 |X_i F|^2,$$

so

$$\|\nabla F\|_\infty \leq \sqrt{3} \max_i \|X_i F\|_\infty \lesssim (1+L) \|F\|_\infty.$$

For the Hessian, in the frame (X_i) one has

$$\text{Hess } F(X_i, X_j) = X_i X_j F - (\nabla_{X_i} X_j) F.$$

Because the metric is bi-invariant,

$$\nabla_{X_i} X_j = \frac{1}{2} [X_i, X_j],$$

and the bracket $[X_i, X_j]$ is a fixed linear combination of X_1, X_2, X_3 with coefficients depending only on the metric normalization. Hence

$$|\text{Hess } F(X_i, X_j)| \lesssim \max_{p,q} |X_p X_q F| + \max_p |X_p F|.$$

Since the operator norm of a bilinear form in a fixed orthonormal basis is controlled by the maximum of its matrix entries, it follows that

$$\|\nabla^2 F\|_{L^\infty} \lesssim \max_{p,q} \|X_p X_q F\|_\infty + \max_p \|X_p F\|_\infty \lesssim (1+L)^2 \|F\|_\infty.$$

This proves the claim. \square

A natural question is whether intermediate bandwidths are beneficial and if so, by how much, compared with making a single big jump from L_0 to L_J . Indeed, frequency marching controls the perturbation induced by higher angular frequencies at the scale of each increment rather than the final bandwidth. A single jump from L_0 to L_J requires to bound the full spectral tail by the curvature of the final high-bandwidth objective; as we show, marching distributes this control over smaller increments.

Since each increment $E_j = F_j - F_{j-1}$ has bandwidth at most L_j , Lemma 3.5 yields

$$a_j \leq B_1 L_j \delta_j, \quad b_j \leq B_2 L_j^2 \delta_j, \tag{16}$$

where we recall that $\delta_j = \|E_j\|_\infty$. This allows to write the assumptions in terms of the quantities $(L_j, \delta_j)_{j=1}^J$.

We let \lesssim absorb the Bernstein constants B_1, B_2 from Lemma 3.5. Suppose we skip all intermediate levels and apply the basin persistence argument directly to the single perturbation $E_{\text{tot}} = F_J - F_0$. Since E_{tot} has bandwidth L_J we have by Lemma 3.5

$$\|\nabla^2 E_{\text{tot}}\|_\infty \lesssim L_J^2 \|E_{\text{tot}}\|_\infty.$$

Preserving strong concavity of the tracked basins therefore is guaranteed by

$$\|E_{\text{tot}}\|_\infty \lesssim \frac{\mu}{L_J^2}. \tag{17}$$

By contrast, when marching we need to apply Lemma 3.5 to each increment E_j separately. Using (16), the condition $\sum_j b_j \leq \mu/2$ from Assumption (B) becomes

$$B_2 \sum_{j=1}^J L_j^2 \delta_j \leq \frac{\mu}{2}.$$

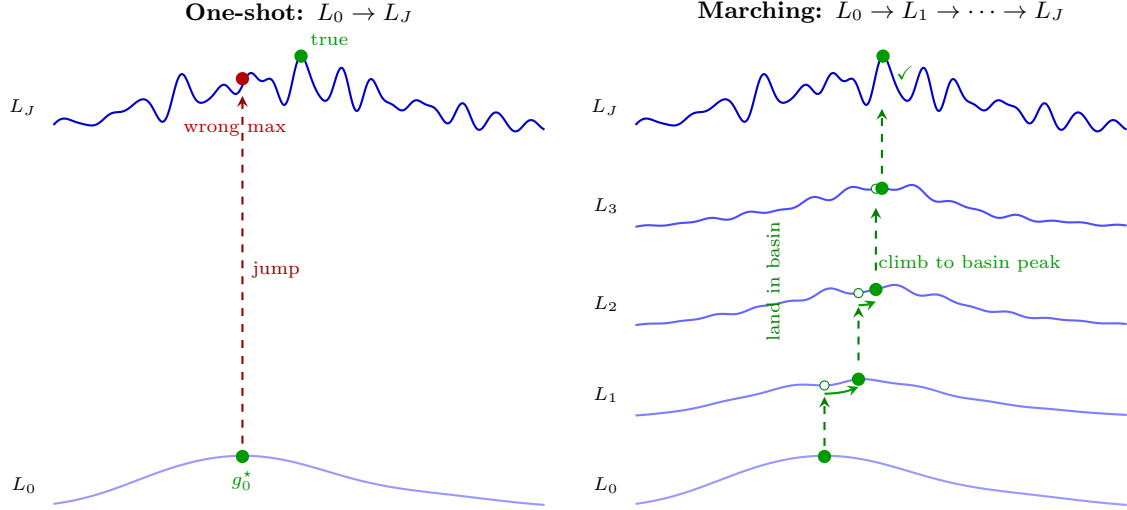


Figure 2: One-shot versus frequency marching on a schematic 1D correlation landscape. **Left:** jumping directly from L_0 to L_J , Newton’s method *can* converge to a spurious local maximum that emerged at high bandwidth. **Right:** under the conditions of Theorem 3.4, marching through intermediate bandwidths keeps the tracked maximizer in the correct basin at each level; Newton refines within the basin before proceeding to the next bandwidth.

Write $\delta_{\text{tot}} = \sum_j \delta_j$ and define the energy-weighted effective bandwidth

$$\bar{L}_2^2 \stackrel{\text{def.}}{=} \frac{\sum_{j=1}^J L_j^2 \delta_j}{\delta_{\text{tot}}}, \quad (18)$$

so that the marching condition reads $\delta_{\text{tot}} \lesssim \mu/\bar{L}_2^2$. Note that $\delta_{\text{tot}} \geq \|E_{\text{tot}}\|_\infty$ by the triangle inequality, so the marching analysis works with a potentially larger numerator. The gain comes from the denominator: since $\bar{L}_2 \leq L_J$, with equality only when all energy is concentrated at the final level, marching compensates by replacing the worst-case L_J^2 weight with the effective weight \bar{L}_2^2 . The denominator improves from L_J^2 to \bar{L}_2^2 , but this can be offset by the larger numerator $\delta_{\text{tot}} = \sum_j \delta_j$. Hence marching is most advantageous when the spectral increments are concentrated at low bandwidths (which is the typical regime for smooth signals or noise-dominated high-frequency content) and the cancellation factor $\delta_{\text{tot}}/\|E_{\text{tot}}\|_\infty$ is not too large. An analogous comparison holds for the gradient-based conditions. The one-shot approach is ensured by $\|E_{\text{tot}}\|_\infty \lesssim \mu r/L_J$, whereas marching imposes two per-step conditions: $L_j \delta_j \lesssim \mu r$ (to apply basin persistence at each level) and $\sum_j L_j \delta_j \lesssim \mu r$ (to control the cumulative drift of the tracked maxima). Both are easier to satisfy when the increments δ_j decay with j .

A toy model. To quantify the gain, consider an example of uniform bandwidth steps $L_j = L_0 + (j-1)\Delta$ with geometrically decaying increments $\delta_j = \delta q^{j-1}$, $q \in (0, 1)$. A direct computation in the $J \rightarrow \infty$ limit gives

$$\bar{L}_2^2 = L_0^2 + \frac{2L_0\Delta q}{1-q} + \frac{\Delta^2 q(1+q)}{(1-q)^2}. \quad (19)$$

The key observation is that this expression is *independent of L_J* : no matter how large the final bandwidth, the effective penalty depends only on L_0 and the decay rate q . When $q \ll 1$ (rapid spectral decay), $\bar{L}_2 \approx L_0$, and the (a priori) marching requirement $\delta_{\text{tot}} \lesssim \mu/L_0^2$ is generically much milder than the one-shot requirement (17). Note that the final suboptimality bound in Theorem 3.4 still scales with L_J^2 , since it reflects the curvature of the final objective rather than the cumulative perturbation.

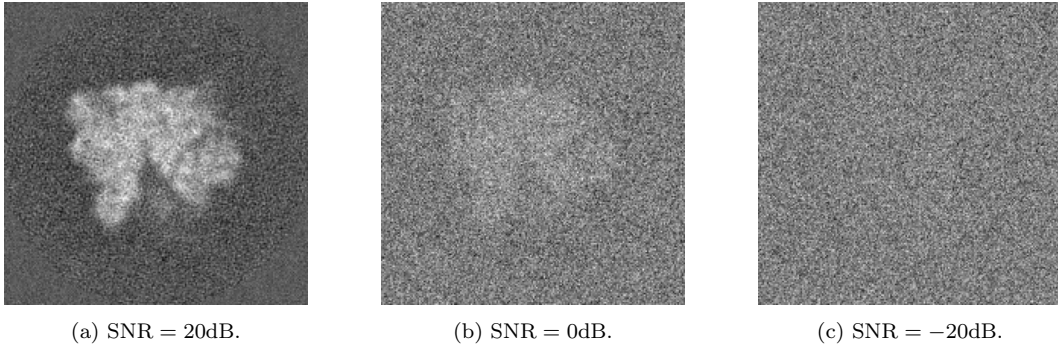


Figure 3: Slice of a ribosome volume corrupted by Gaussian noise at the indicated SNR levels.

4 Experiments

We first validate the proposed method on synthetic data, demonstrating substantial gains in both speed and accuracy over exhaustive rotational search. We then show that our approach can be used as a drop-in replacement in the subtomogram averaging (STA) pipeline of RELION, accelerating rotational alignment by an order of magnitude while refining a ribosome to 4\AA , reaching the local Nyquist limit of 3.8\AA .

The experiments were conducted either on one A100-80GB GPU (Section 4.1) or on four RTX4090 GPUs (Section 4.2). They can be reproduced using code available at <https://github.com/swing-research/Matcha>

4.1 Rotational search: synthetic examples

Let $h \in \mathbb{R}^{N \times N \times N}$ denote a ribosome density at 13\AA resolution (EMDB:EMD-3228), obtained from the EMPIAR-10045 dataset¹. We synthetically generate measurements

$$f = g^* \circ h + \eta,$$

where $g^* \in \text{SO}(3)$ is the ground truth rotation (assumed unknown in the search) and η is additive white Gaussian noise. We consider three signal-to-noise ratios: 20 dB, 0 dB, and -20 dB. Figure 3 shows a representative volume slice at each level; at 0 dB the signal and noise have equal energy, and in cryogenic electron microscopy it is common to work at or below -20 dB. We report the results at 0 dB in the main text and defer the remaining SNR levels to Appendix B.2.

At each SNR, we generate 1000 randomly rotated volumes of size $N = 200$ and compare the performance of Algorithm 1 with SOFFT [4, 18, 7]. SOFFT evaluates the cross-correlation on a discrete grid of rotations whose resolution is controlled by an oversampling factor K : increasing K refines the grid at the cost of evaluating $(K - 1)^3$ additional points. All SOFFT experiments were run with a batch size of one, as larger batches exceed GPU memory at higher bandwidths; even so, SOFFT frequently produces out-of-memory errors at large oversampling factors (see Figure 4b).

For Matcha, we select 10 candidate rotations as the highest local maxima of the cross-correlation computed by SOFFT at a coarse bandwidth $L_0 = 30$ with oversampling factor 2. Candidates are then refined across bandwidth $L_j \in \{30, 40, 60, L_{\max}\}$, skipping any L_j that exceed L_{\max} : at each L_j , a single Newton step is applied to every candidate, and refined estimates are propagated to the next band. After optimization at L_{\max} , the candidate with the highest correlation score is retained.

Figure 4a reports the wall-clock time and 90th-percentile alignment error for a fixed bandwidth $L_{\max} = 40$, which yields the fastest inference but not the best resolution—especially for SOFFT, whose accuracy is fundamentally limited by its grid spacing. At the highest oversampling factor that does not cause out-of-memory errors ($K = 18$), SOFFT achieves 0.13° accuracy but requires over a hundred seconds. For $K = 8$ and above, wall-clock times range from ten seconds to several minutes. By contrast, Matcha achieves 0.03° accuracy—over four times more precise—within a few seconds, despite starting from a coarse initial grid.

¹<https://www.ebi.ac.uk/emdb/EMD-3228>

This gain stems from a structural advantage: unlike SOFFT, whose accuracy is fundamentally limited by the grid spacing at a given bandwidth, Matcha uses the grid only to identify candidate basins and then refines continuously to a precision that is independent of the initial grid resolution.

Matcha also uses memory more efficiently, which enables larger batch sizes when processing multiple volumes. Under identical hardware constraints, SOFFT is limited to a batch size of 10 for $K \leq 8$, a batch size of 4 for $K = 10$, and a batch size of 1 for $K = 18$, whereas Matcha supports batch sizes of up to 100.

The maximum bandwidth L_{\max} is a key hyperparameter of both methods: small values yield fast computation but introduce bias that limits accuracy, while larger values are slower but more accurate. Figure 4b confirms that higher L_{\max} consistently improves estimation accuracy. The effect is moderate for Matcha and more pronounced for SOFFT at all oversampling factors. Beyond $L_{\max} = 100$, improvements for Matcha are marginal, whereas SOFFT becomes infeasible due to memory constraints.

We also compare the Newton refinement used in Matcha with a first-order gradient method. Since both methods require evaluating the same band-limited objective, the practical difference is the number of refinement steps needed to reach high precision. Figure 4c shows that Newton refinement reaches close to optimal accuracy after very few steps, whereas the first-order method requires much more steps for the desired accuracy. This supports our use of one Newton step per bandwidth level in the synthetic experiments.

4.2 Nyquist resolution in cryo-ET using STA

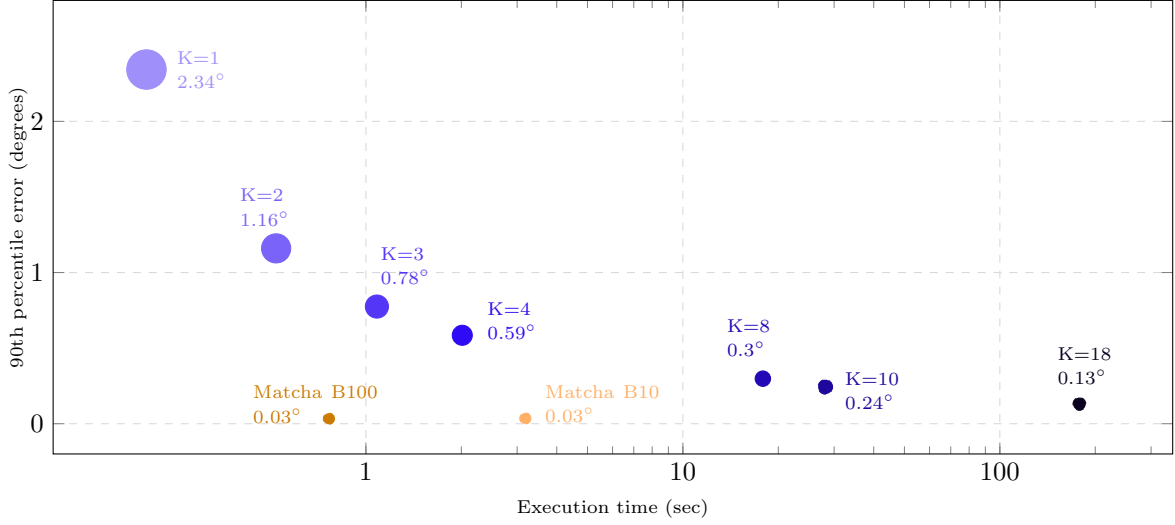
We integrate Matcha into the subtomogram averaging pipeline of RELION5 [19] as a drop-in replacement for the rotational alignment performed during *3D auto-refine*. All other processing steps (classification, CTF-refinement, Bayesian polishing) remain unchanged and are executed using RELION’s own implementation throughout; since these steps are shared between the baseline and our method, we exclude them from the runtime comparison and report only the cumulative wall-clock time spent on alignment.

We follow the STA tutorial² for the Chlamy dataset (EMPIAR-11830), originally published by [20]. The dataset contains 33 bin4 tomograms, from which 20,990 particles were extracted using *pytom-match-pick* [21]. The RELION baseline refines progressively through three binning levels (bin4, bin2, bin1), reaching 3.8 Å local resolution at bin1—the Nyquist limit—under gold-standard FSC at a threshold of 0.143. The cumulative alignment time across all three stages is approximately 3.5 hours on four RTX 4090 GPUs.

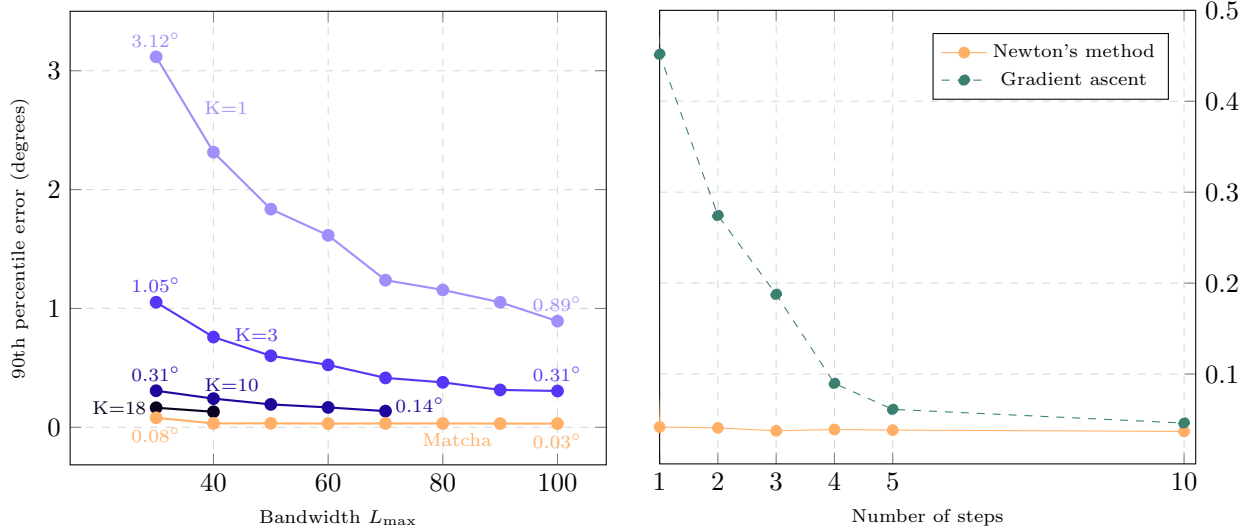
We replace *3D auto-refine* at the bin2 and bin1 stages, retaining RELION’s bin4 alignment as initialization. Matcha estimates both rotations and translations using the same half-set split as RELION, with translations recovered via FFT-based correlation (details in Appendix C). At each binning level, we perform $T = 3$ outer rotation–translation alternations. Within each alternation, we retain $N_C = 10$ rotation candidates from a local search at angular cutoff $L_0 = 30$ with oversampling factor 2, and refine with $M = 5$ Newton steps—more conservative than the 1–2 steps sufficient in the synthetic setting (Section 4.1), to ensure convergence under the noisier conditions of experimental data—through bandwidths $\{30, 40, L_{\max}\}$, where $L_{\max} = 45$ (bin2) and $L_{\max} = 60$ (bin1). Shifts are estimated via FFT-based correlation with subpixel refinement [22].

Our bin1 reconstruction attains 3.8 Å local resolution (Nyquist), identical to the RELION baseline, and 4.0 Å global resolution under the same FSC criterion. The cumulative alignment time drops from approximately 3.5 hours (RELION) to roughly 20 minutes (Matcha), a speedup of over 10× (Figure 5). Since the non-alignment processing steps add a fixed overhead of approximately 90 minutes to both pipelines, the end-to-end speedup is smaller but alignment is the dominant cost in standard STA workflows.

²<https://tomoguide.github.io>



(a) Accuracy vs. execution time ($L_{\max} = 40$).



(b) Effect of L_{\max} for varying oversampling K .

(c) Newton's method vs. gradient ascent ($L_{\max} = 40$).

Figure 4: Hyperparameter study for Matcha and SOFFT at SNR = 0 dB. In (a), dot size encodes alignment error; Matcha achieves 0.03° accuracy in seconds, whereas SOFFT at its highest feasible oversampling ($K = 18$) requires over a hundred seconds for 0.13°. In (b), increasing L_{\max} improves both methods, but the effect is more pronounced for SOFFT; beyond $L_{\max} = 100$, SOFFT becomes memory-prohibitive at large K . In (c), a single Newton step matches the accuracy that gradient ascent reaches only after several iterations, supporting the use of one Newton step per band in (a) and (b).

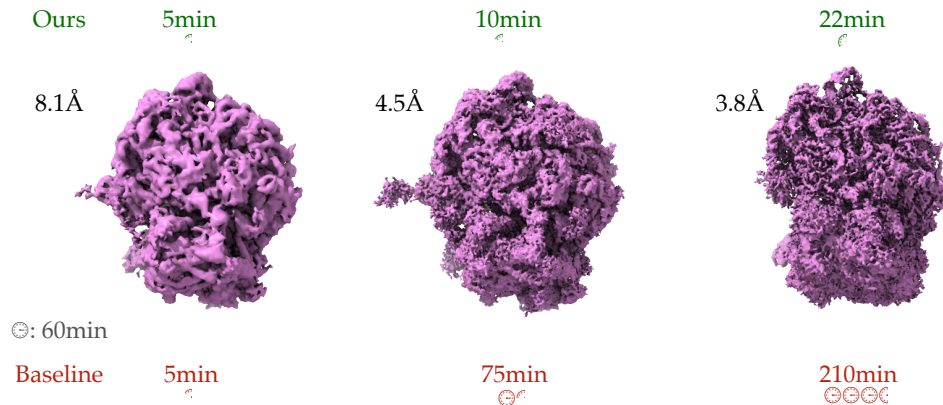


Figure 5: Subtomogram averaging on the Chlamy dataset (EMPIAR-11830) using RELION5. Matcha replaces *3D auto-refine* at the bin2 and bin1 stages, matching the baseline resolution (3.8 Å at Nyquist) while reducing cumulative alignment time by over 10×. Intermediate processing steps (CTF-refinement, classification, template updates) are shared between both pipelines and excluded from the reported timings.

5 Conclusion

We presented Matcha, a frequency-marching algorithm for fast rotational alignment that replaces exhaustive high-resolution search with a combination of coarse $SO(3)$ -FFT initialization and Newton refinement across progressively finer angular bandwidths. The key algorithmic insight is that band-limited correlation landscapes are smooth enough for second-order optimization to converge in very few steps, while the low-dimensional structure of $SO(3)$ keeps the per-step cost negligible. The key theoretical insight is that frequency marching—refining through intermediate bandwidths rather than jumping directly to the target resolution—relaxes the spectral-decay conditions required for provable basin tracking from a worst-case L_J^2 scaling to an effective \bar{L}_2^2 scaling that is independent of the final bandwidth.

On synthetic benchmarks, Matcha achieves sub-degree angular accuracy several orders of magnitude faster than exhaustive search. Integrated into the RELION5 subtomogram averaging pipeline, it reduces alignment runtime by over 10× while matching Nyquist-limited reconstruction quality, demonstrating that the approach is practical for large-scale cryo-ET datasets.

Several directions remain open. First, our convergence analysis assumes a deterministic setting with known signal structure; it would be valuable to establish probabilistic guarantees—for instance, showing that the spectral-decay and gap conditions hold with high probability over a suitable ensemble of noisy particles. Second, the current alternating rotation–translation scheme inherits the limitations of block coordinate ascent. A joint continuous optimization over the full six-dimensional pose space, exploiting the semi-direct product structure of $SE(3)$, could improve both accuracy and convergence speed. Third, the image formation model in cryo-ET includes degradations beyond additive noise—notably the contrast transfer function (CTF) and the missing wedge—which are currently handled between alignment iterations rather than within them. Incorporating these effects directly into the band-limited correlation objective could potentially reduce the number of outer iterations needed and further accelerate the pipeline. Finally, in practice the reference template is itself unknown and must be iteratively estimated from the data, and the particle population may contain multiple conformational states. The speed of Matcha makes it feasible to evaluate alignment against multiple candidate templates per iteration, opening a path toward faster heterogeneity analysis in subtomogram averaging.

A Ball harmonics, rotational correlation, and radial sparsity

The ball harmonics provide an orthonormal, rotation-steerable basis for the function space $L^2(\mathcal{B}_3)$ that is naturally ordered by Laplacian eigenvalues. This structure makes the representation particularly convenient for rotational alignment via cross-correlation, and it induces a characteristic *radial sparsity* pattern under the eigenvalue-based truncation used as described in [8].

In this part, we give more precise definition of the ball harmonics, their properties and we provide references for the main results.

A.1 Ball harmonics expansion and eigenvalue-based truncation

We let \mathcal{B}_3 denote the unit ball in \mathbb{R}^3 and let $u : \mathcal{B}_3 \rightarrow \mathbb{R}$ be supported on \mathcal{B}_3 . It admits an expansion of the form

$$u(x) = \sum_{(k,\ell,m) \in \mathcal{I}_\Lambda} \hat{u}_{k,\ell,m} \psi_{k,\ell,m}(x), \quad (20)$$

where the basis $\{\psi_{k,\ell,m}\}_{k,\ell,m}$ is known as the ball harmonics basis. These basis functions are separable into radial (indexed by k) and angular (indexed by (ℓ, m)) factors and form an orthonormal basis of $L^2(\mathcal{B}_3)$, see [8] for conventions. The basis functions $\{\psi_{k,\ell,m}\}_{k,\ell,m}$ are Dirichlet Laplacian eigenfunctions on \mathcal{B}_3 with eigenvalues/frequencies $\lambda_{\ell k} = j_{\ell,k}$, the k th positive root of the spherical Bessel function j_ℓ , and satisfy the eigenvalue equation

$$-\Delta \psi_{k,\ell,m} = \lambda_{\ell k}^2 \psi_{k,\ell,m} \quad \text{in } \mathcal{B}_3,$$

with $\psi_{k,\ell,m} = 0$ on $\partial\mathcal{B}_3$. In practice, we keep only frequencies $\lambda_{\ell k}$ that are below a certain threshold (frequency budget) $\Lambda > 0$, and retain the index set

$$\mathcal{I}_\Lambda := \{(k, \ell, m) : \lambda_{\ell k} \leq \Lambda, \ell \in \mathbb{Z}_{\geq 0}, m \in \{-\ell, \dots, \ell\}, k \in \mathbb{Z}_{>0}\}.$$

For a given angular degree ℓ , define the retained radial set

$$K_\ell := \{k \in \mathbb{Z}_{>0} : \lambda_{\ell k} \leq \Lambda\}.$$

The function $(\ell, k) \mapsto \lambda_{\ell k}$ is increasing in both ℓ and k , so the cardinality $|K_\ell|$ decrease monotonically with ℓ . Low-rank approximation can be employed to reduce the number of coefficients in the set \mathcal{I}_Λ , see Appendix B.1.

A.2 Computational complexity

A key practical property is that the truncated expansion in Equation (20) can be computed in nearly-linear time (up to polylogarithmic factors) in the number of voxels.

Lemma A.1 (Ball harmonics transform complexity). *Given a volume sampled on an $N \times N \times N$ Cartesian grid, the ball harmonics decomposition up to a bandwidth $\Lambda = \mathcal{O}(N)$ can be computed with complexity $\mathcal{O}(N^3 \log^2 N)$ while achieving numerical accuracy $\varepsilon = \mathcal{O}(1/N)$.*

Proof. This follows from [8, Theorem 3.1]. Choosing $\varepsilon = 1/N$ gives $|\log \varepsilon| = \Theta(\log N)$, so the stated complexity bound reduces to $\mathcal{O}(N^3(\log N)^2)$ for $\Lambda = \mathcal{O}(N)$. \square

A.3 Wigner– D matrices

An orthogonal basis for $L^2(\text{SO}(3))$ is given by the Wigner D -matrices. As a result, rotation of ball harmonic functions can be expressed as a linear combination of other ball harmonic functions and Wigner D -matrices with angular indices up to the same order. This property will become handy to efficiently evaluate the cross-correlation for a large number of rotations, as well as for calculating their first and second order derivatives. More precisely, for any $g \in \text{SO}(3)$, we have

$$\psi_{k,\ell,m}(g^{-1}x) = \sum_{m'=-\ell}^{\ell} D_{mm'}^\ell(g) \psi_{k,\ell,m'}(x), \forall x \in \mathcal{B}_3.$$

As defined in Equation 3, any rotation $g \in \text{SO}(3)$ can be parameterized by ZYZ Euler angles $(\alpha, \beta, \gamma) \in [0, 2\pi) \times [0, \pi] \times [0, 2\pi)$. For each angular degree $\ell \in \mathbb{Z}_{\geq 0}$, the Wigner D -matrix

$$D^\ell(g) \in \mathbb{C}^{(2\ell+1) \times (2\ell+1)},$$

has entries indexed by order $m, m' \in \{-\ell, \dots, \ell\}$ and is defined by

$$D_{mm'}^\ell(\alpha, \beta, \gamma) = e^{-im\alpha} d_{mm'}^\ell(\beta) e^{-im'\gamma}, \quad (21)$$

where $d_{mm'}^\ell$ are the *Wigner d -functions*. The Wigner d -functions depend only on the polar angle β and admit explicit expressions in terms of finite sums [23] and can be evaluated efficiently.

The collection $\{D_{mm'}^\ell\}_{\ell, m, m'}$ forms an orthogonal basis of $L^2(\text{SO}(3))$ with respect to the Haar measure dg , normalized so that

$$\int_{\text{SO}(3)} D_{mm'}^\ell(g) \overline{D_{nn'}^{\ell'}(g)} dg = \frac{1}{8\pi^2} \delta_{\ell\ell'} \delta_{mn} \delta_{m'n'}. \quad (22)$$

The Wigner D -matrices admit closed-form expressions not only for their values but also for their derivatives with respect to the rotation parameters. In particular, derivatives with respect to the Euler angles (α, β, γ) can be written analytically in terms of the same Wigner D -matrices, see [23]. Differentiation with respect to α and γ acts diagonally,

$$\partial_\alpha D_{mm'}^\ell = -im D_{mm'}^\ell, \quad \partial_\gamma D_{mm'}^\ell = -im' D_{mm'}^\ell,$$

while derivatives with respect to β can be expressed as finite linear combinations of $d_{mm'}^\ell(\cos \beta)$ with shifted indices and known coefficients. As a result, gradients and higher-order derivatives of Wigner D -matrices are available analytically and can be evaluated efficiently.

A.4 Rotational cross-correlation in the ball harmonics basis

Rotations act only on the angular index via Wigner- D matrices. Consequently, the rotational cross-correlation of $f, h \in L^2(\mathcal{B}_3)$,

$$C(g) = \int_{\mathcal{B}_3} f(x) \overline{h(R_g^{-1}x)} dx, \quad g \in \text{SO}(3),$$

admits a natural Wigner- D expansion. In a band-limited setting with angular cutoff L , we write

$$C_L(g) = \sum_{\ell=0}^L \sum_{m=-\ell}^{\ell} \sum_{m'=-\ell}^{\ell} \sigma_{\ell mm'} D_{mm'}^\ell(g),$$

where $D_{mm'}^\ell(g)$ are the Wigner- D matrix entries defined in Equation (21). The coefficients are determined directly by the ball harmonic coefficients of f and h :

$$\sigma_{\ell mm'} = \sum_{k \in K_\ell} \hat{f}_{k, \ell, m} \overline{\hat{h}_{k, \ell, m'}}.$$

We will see that these coefficients admit a low-dimension decomposition.

A.5 Low-rank structure induced by radial sparsity

For each fixed ℓ , define the $(2\ell + 1) \times (2\ell + 1)$ matrix

$$A_\ell = [\sigma_{\ell mm'}]_{m, m' = -\ell}^\ell.$$

Using (A.4), A_ℓ admits the factorization

$$A_\ell = \sum_{k \in K_\ell} a_{\ell k} b_{\ell k}^*, \quad (a_{\ell k})_m = \hat{f}_{k, \ell, m}, \quad (b_{\ell k})_m = \hat{h}_{k, \ell, m}, \quad (23)$$

and therefore

$$\text{rank}(A_\ell) \leq |K_\ell|. \quad (24)$$

Since eigenvalue-based truncation enforces $|K_\ell|$ to decrease with ℓ , the coefficients blocks A_l of the correlation become progressively low-rank at higher angular degrees. In practice, the effective rank is often even smaller than $|K_l|$ due to additional dependencies among the vectors $\{a_{\ell k}\}_{k \in K_\ell}$ and $\{b_{\ell k}\}_{k \in K_\ell}$.

In particular, $\text{rank}(A_l)$ does not depend on the rotation of h : Let $h_{g^*} = h(R_{g^*}^{-1}x)$ be the volume h rotated by $g^* \in \text{SO}(3)$ with $(b_{\ell k})_m^{(g^*)}$ and $A_l^{(g^*)}$ the corresponding factorization of the ball harmonics coefficients of h_{g^*} . Since

$$A_l^{(g^*)} = \sum_k a_{\ell k} b_{\ell k}^{*(g^*)} = \sum_k a_{\ell k} b_{\ell k}^* D^l(g^*)^\dagger = A_l D^l(g^*)^\dagger.$$

and because the matrices $D^l(g)$ are unitary, and hence invertible, for any $g \in \text{SO}(3)$, we have

$$\text{rank}(A_l^{(g^*)}) = \text{rank}(A_l D^l(g^*)^\dagger) = \text{rank}(A_l) \leq |K_l|.$$

B Additional Experiments

B.1 Empirical effective rank of Wigner blocks versus the theoretical bound

In Appendix A.5 we remark that, for each angular degree l , the Wigner block $A_l \in \mathbb{C}^{(2l+1) \times (2l+1)}$ of the rotational correlation admits a factorization such that $\text{rank}(A_l) \leq |K_l|$, where K_l is the set of radial indices retained at degree l by the eigenvalue cutoff Λ . This provides a *theoretical* (worst-case) rank upper bound determined purely by the truncation scheme. In practice, however, we observe substantially lower rank behavior.

For selected degrees $l \in \{20, 30, 50, 80\}$, see Figure 6a, the singular values exhibit a pronounced spectral gap: only a small number of modes carry significant mass, while the remaining singular values rapidly decay to a near-zero floor. Motivated by this behavior, we define the effective rank as

$$r_{\text{eff}}(l) \stackrel{\text{def.}}{=} \min\{k : \frac{s_{k+1}(A_l)}{s_k(A_l)} < \rho\},$$

where $s_1(A_l) \geq s_2(A_l) \geq \dots$ are the singular values of A_l and ρ is a fixed numerical tolerance.

Figure 6b shows $r_{\text{eff}}(l)$ alongside the upper-bound $|K_l|$ across degrees for $\rho = 0.2$. Across degrees, $r_{\text{eff}}(l)$ stays well below $|K_l|$ with high- l blocks approaching rank one. This indicates that the correlation is effectively supported on a low-dimensional subspace relative to the ambient $(2l+1) \times (2l+1)$ block size.

B.2 Ablation study for other noise regimes

We follow the experimental setting presented in Section 4.1 and display the results for the extremely noisy setting, SNR=-20dB, and the easier setting, SNR=20dB.

A key hyperparameter of Matcha and SOFFT is the maximum bandwidth L_{max} used to evaluate the truncated correlation in Equation (5). This parameter controls the highest angular frequencies included in the alignment score and trades high-resolution information for computational time.

With Matcha, the experiments indicate that accurate alignment can already be achieved at relatively low bandwidth when the signal-to-noise ratio is moderate or high. As shown in Figures 4b, the alignment accuracy remains high across the entire range of tested L_{max} , suggesting that low-frequency components alone are sufficient to reliably localize the correct rotation in these regimes.

At very low SNR, e.g. SNR = -20 dB, Figure 7b, the overall accuracy of both methods degrades, reflecting the increased difficulty of the alignment problem. Nevertheless, both methods continue to benefit from increasing the bandwidth. For Matcha, higher values of L_{max} lead to a gradual improvement in accuracy even in this strongly noisy setting, although the gains become progressively smaller as additional high-frequency components are increasingly dominated by noise. A similar trend is observed for SOFFT.

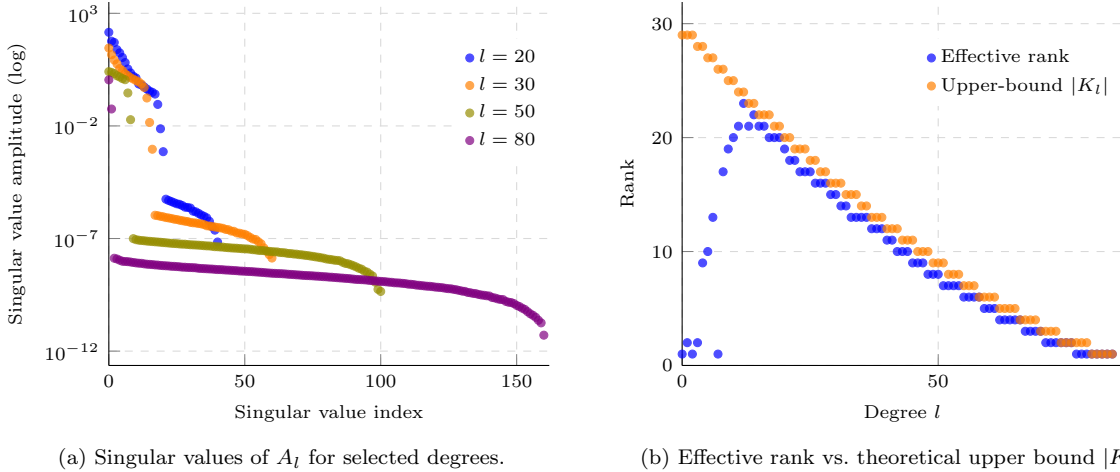


Figure 6: Spectral properties of the Wigner blocks A_l . In (a), the singular values exhibit a sharp spectral gap at each degree, with only a few modes carrying significant energy. In (b), the effective rank (defined by the ratio criterion $s_{k+1}/s_k < \rho$ with $\rho = 0.2$) stays well below the theoretical bound $|K_l|$ across all degrees, with high- l blocks approaching rank one. This low-rank structure can be exploited to accelerate the evaluation of C_L .

Overall, these results show that, as expected, increasing the bandwidth is beneficial for both methods across all noise levels. At the same time, Matcha exhibits strong robustness to bandwidth truncation at moderate and high SNR, achieving high accuracy even at low L_{\max} , while still being able to exploit additional frequency information when available.

Figure 7a and Figure 7b present the execution times for Matcha and SOFFT with varying oversampling factor K at SNR 20dB and -20dB respectively. In general, execution time for both Matcha and SOFFT does not depend on the noise level.

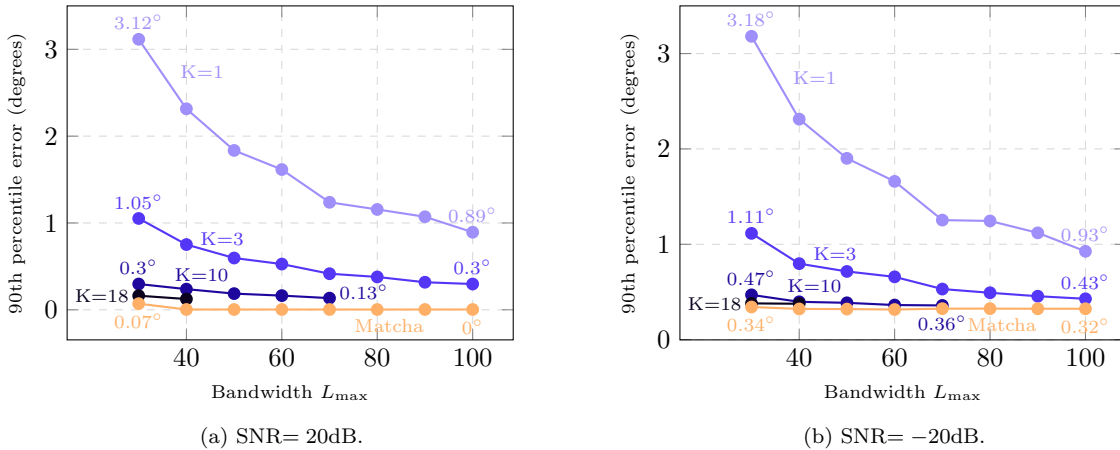


Figure 7: Alignment accuracy of Matcha and SOFFT with varying oversample factor K for different L_{\max} for different SNR.

C Alternating search over rotations and translations

In subtomogram alignment, the relative pose between two volumes is typically described by a rotation and a translation. Given two volumetric densities $f, h \in L^2(\mathcal{B}^3)$, we consider the *6-dimensional alignment problem*

$$(\hat{\tau}, \hat{g}) \in \underset{\tau \in \mathbb{R}^3, g \in \text{SO}(3)}{\text{argmax}} C(\tau, g), \quad C(\tau, g) \stackrel{\text{def}}{=} \langle f, g \circ \mathcal{S}_\tau h \rangle, \quad (25)$$

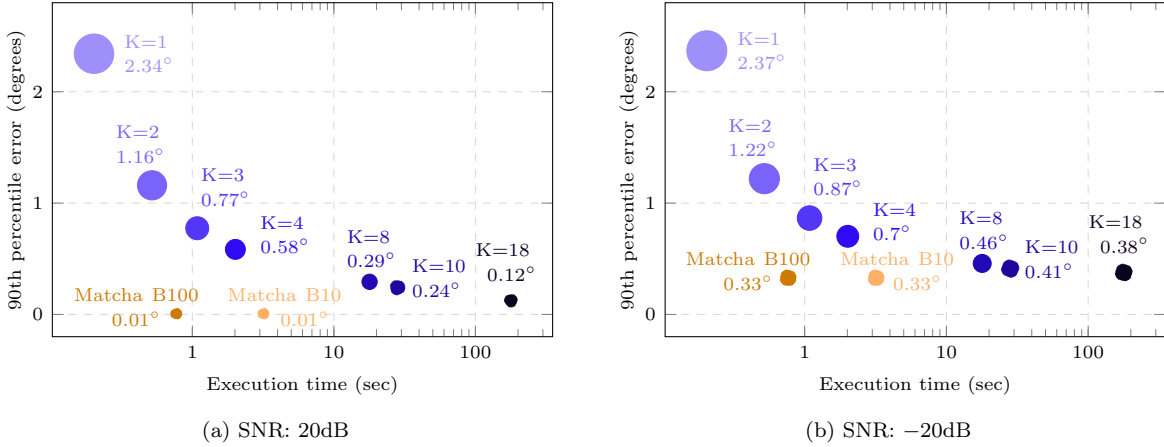


Figure 8: Alignment accuracy of Matcha and SOFFT versus execution time for $L_{max} = 40$ and varying SNR. Large dot sizes correspond to larger alignment error. Matcha is one order of magnitude more precise and several orders of magnitude faster than exhaustive search SOFFT.

where $(\mathcal{S}_\tau h)(x) = h(x - \tau)$ denotes the translation operator.

It is unrealistic to exhaustively discretize the parametrization of the cross-correlation as defined in Problem (25) as it lives in six dimensions. A common approach is to alternate between optimization over shifts and over the rotations, e.g. [15]. For fixed shift τ , optimization over g can be performed efficiently using Algorithm 1. For fixed rotation g , the optimal translation can be estimated efficiently on a fine grid by evaluating the cross-correlation with 3D FFT.

More precisely, we start from zero shift and estimate the rotation using Algorithm 1. Then, given the estimated rotation, we estimate the translation of the rotated volume via a 3D FFT-based correlation. This alternating process is repeated for a small number of iterations, e.g. $T = 3$ in the experiment of Section 4.2.

Remarks. (i) Each translation update costs $\mathcal{O}(N^3 \log N)$ on an $N \times N \times N$ grid (or less if restricted to a bounded search window), and is typically inexpensive compared to the rotation refinement at higher angular cutoffs. (ii) The outer loop is a block coordinate ascent method and is not guaranteed to find the global maximizer of the 6-dimensional objective; nevertheless, empirically, it has been employed successfully and is known to be robust if relatively accurate initial translation is provided. (iii) If desired, multi-resolution translation refinement can be employed to achieve sub-pixel accuracy, for example using the efficient upsampled phase-correlation scheme of [22]. (iv) Translational search can be restricted to a local neighborhood if an accurate initial translation is available; as is the case for the hierarchical binning refinement data typically employed in STA, see Experiment 4.2.

References

- [1] George L. Turin. An introduction to matched filters. *IRE Transactions on Information Theory*, 6(3):311–329, 1960.
- [2] Steven M. Kay. *Fundamentals of Statistical Signal Processing, Volume II: Detection Theory*. Prentice Hall, 1998.
- [3] Valentin Debarnot and Pierre Weiss. Blind inverse problems with isolated spikes. *Information and Inference: A Journal of the IMA*, 12(1):26–71, 2023.
- [4] Peter J. Kostelec and Daniel N. Rockmore. FFTs on the Rotation Group. *Journal of Fourier Analysis and Applications*, 14(2):145–179, April 2008.
- [5] Matthew A. Price and Jason D. McEwen. Differentiable and accelerated spherical harmonic and Wigner transforms. *Journal of Computational Physics*, 510:113109, August 2024.

- [6] Julio A Kovacs and Willy Wriggers. Fast rotational matching. *Biological Crystallography*, 58(8):1282–1286, 2002.
- [7] Jason D McEwen, Martin Büttner, Boris Leistedt, Hiranya V Peiris, and Yves Wiaux. A novel sampling theorem on the rotation group. *IEEE Signal Processing Letters*, 22(12):2425–2429, 2015.
- [8] Joe Kileel, Nicholas F Marshall, Oscar Mickelin, and Amit Singer. Fast expansion into harmonics on the ball. *SIAM Journal on Scientific Computing*, 47(2):A1117–A1144, 2025.
- [9] Yu-hsuan Shih, Garrett Wright, Joakim Andén, Johannes Blaschke, and Alex H Barnett. cufinufft: a load-balanced gpu library for general-purpose nonuniform ffts. In *2021 IEEE International Parallel and Distributed Processing Symposium Workshops (IPDPSW)*, pages 688–697. IEEE, 2021.
- [10] Julio A Kovacs, Pablo Chacón, Yao Cong, Essam Metwally, and Willy Wriggers. Fast rotational matching of rigid bodies by fast fourier transform acceleration of five degrees of freedom. *Biological Crystallography*, 59(8):1371–1376, 2003.
- [11] Leandro Farias Estrozi and Jorge Navaza. Fast projection matching for cryo-electron microscopy image reconstruction. *Journal of Structural Biology*, 162(2):324–334, 2008.
- [12] A. Bartesaghi, P. Sprechmann, J. Liu, G. Randall, G. Sapiro, and S. Subramaniam. Classification and 3D averaging with missing wedge correction in biological electron tomography. *Journal of Structural Biology*, 162(3):436–450, June 2008.
- [13] Maxim Shatsky, Pablo Arbelaez, Robert M Glaeser, and Steven E Brenner. Optimal and fast rotational alignment of volumes with missing data in fourier space. *Journal of Structural Biology*, 184(2):345–347, 2013.
- [14] Min Xu, Martin Beck, and Frank Alber. High-throughput subtomogram alignment and classification by fourier space constrained fast volumetric matching. *Journal of structural biology*, 178(2):152–164, 2012.
- [15] Yuxiang Chen, Stefan Pfeffer, Thomas Hrabe, Jan Michael Schuller, and Friedrich Förster. Fast and accurate reference-free alignment of subtomograms. *Journal of Structural Biology*, 182(3):235–245, June 2013.
- [16] Mona Zehni, Laurène Donati, Emmanuel Soubies, Zhizhen Zhao, and Michael Unser. Joint angular refinement and reconstruction for single-particle cryo-em. *IEEE Transactions on Image Processing*, 29:6151–6163, 2020.
- [17] Alex Barnett, Leslie Greengard, Andras Pataki, and Marina Spivak. Rapid solution of the cryo-em reconstruction problem by frequency marching. *SIAM Journal on Imaging Sciences*, 10(3):1170–1195, 2017.
- [18] Daniel Potts, Jürgen Prestin, and Antje Vollrath. A fast algorithm for nonequispaced Fourier transforms on the rotation group. *Numerical Algorithms*, 52(3):355–384, November 2009.
- [19] Alister Burt, Bogdan Toader, Rangana Warshamanage, Andriko von Kügelgen, Euan Pyle, Jasenko Zivanov, Dari Kimanius, Tanmay AM Bharat, and Sjors HW Scheres. An image processing pipeline for electron cryo-tomography in relion-5. *FEBS open bio*, 14(11):1788–1804, 2024.
- [20] Ron Kelley, Sagar Khavnekar, Ricardo D Righetto, Jessica Heebner, Martin Obr, Xianjun Zhang, Saikat Chakraborty, Grigory Tagiltsev, Alicia K Michael, Sofie Van Dorst, et al. Toward community-driven visual proteomics with large-scale cryo-electron tomography of chlamydomonas reinhardtii. *Molecular Cell*, 86(1):213–230, 2026.
- [21] Marten L. Chaillet, Sander Roet, Remco C. Veltkamp, and Friedrich Förster. pytom-match-pick: A tophat-transform constraint for automated classification in template matching. *Journal of Structural Biology: X*, 11:100125, June 2025.
- [22] Manuel Guizar-Sicairos, Samuel T. Thurman, and James R. Fienup. Efficient subpixel image registration algorithms. *Optics Letters*, 33(2):156–158, January 2008.

- [23] V. K. Khersonskii, A. N. Moskalev, and D. A. Varshalovich. *Quantum Theory Of Angular Momentum*. World Scientific Publishing Company, 1988. Accepted: 2021-08-20T11:39:57Z.